2016

Investigation Of Hydrate Growth Rate On The Interface Between Liquid and Solid Film

Hongxia Zhou
Technology University of Delft, The Netherlands,, h.zhou-1@tudelft.nl

Carlos Infante Ferreira
Technology University of Delft, The Netherlands,, C.A.InfanteFerreira@tudelft.nl

Investigation of hydrate growth rate on the interface between liquid and solid film

Hongxia ZHOU*; Carlos INFANTE FERREIRA

Leeghwaterstraat 39, P&E Department, 3ME

Delft University of Technology, the Netherlands

*Corresponding Author: h.zhou-1@tudelft.nl

ABSTRACT

Hydrate slurry has been reported to be a suitable secondary fluid for refrigeration and air-conditioning systems. The latent heat of CO_2 hydrate is 387 kJ/kg under phase equilibrium condition of 7 °C and 30 bar. The utilization of CO_2 hydrate slurry in air-conditioning systems is promising in improving the energy efficiency and shifting energy supply and demand load as well as relieving greenhouse effect caused by normal refrigerants like CFCs, HCFCs etc.

The production of CO_2 hydrate slurry in a coil heat exchanger is investigated in this study. Crystals are supposed to firstly form on the wall of the tube, generating a solid layer. The appearance of the solid layer increases the heat resistance from liquid to the refrigerant. Type-III antifreeze proteins have been added to the solution to better control the crystallization process of hydrate formation since AFPs have proven to be an effective hydrate formation preventer which is environment friendly. A kinetic model is developed based on the gas hydrate growth model of Skovborg and Rusmussen (1994), taking the mass transfer process to be the rate-control step. The influence of pressure, temperature and concentration of the hydrate formation preventer on the diffusion coefficient of dissolved gas into the solid interface is investigated and mainly the concentration of hydrate formation preventer appears to have a large impact.

Results show that the growth rate decreases with the increase of the concentration of AFPs. Higher concentrations of AFPs move the equilibrium line to slightly higher temperatures.

Keywords: hydrate slurry; crystallization; kinetic model.

1. INTRODUCTION

Pumpable phase change materials (PCMs) are one of the most efficient candidates to be applied as secondary cooling fluids due to the large latent heat when undergoing a phase change from solid to liquid or liquid to gas or vice versa, which can substantially increase the energetic and economic performance of secondary cooling systems. Ice slurries have been introduced as secondary cooling fluids in the beginning of the century (Bel and Lallemand, 1999; Tanino and Kozawa, 2001; Ayel et al., 2003; Matsumoto et al., 2004). These systems show improved performance when compared with single-phase secondary refrigerants (Kauffeld et al., 1999). CO_2 hydrate slurry is a favourable secondary fluid which can be applied in air-conditioning systems: it has a large latent heat (387 kJ/kg) and positive phase change temperature (7-8 °C). This allows for the application of primary refrigeration cycles which operate at significantly higher evaporating temperatures than cycles applied in conventional rapid chilling plants. Making use of a latent heat thermal storage system (LHTS), the generation unit runs in a day/night mode, therefore the condensing temperature of the refrigeration cycle can be lowered. In these ways, the refrigeration cycle efficiency is correspondingly significantly improved in comparison with conventional designs.

Formation of gas hydrates in oil and gas pipelines and processing equipment is something that the petroleum industry is most concerned about since it can lead to flow blockage and severe economic loss. A fluidized bed generator has been used to produce CO_2 hydrate slurry continuously as shown by Zhou et al. (2015). However, the construction of such a system with a fluidized bed heat exchanger requires a large investment which is not cost-effective for industry. Simpler generators are expected to significantly improve the economy of these systems. In

this study, a coil heat exchanger is proposed to produce CO_2 hydrate slurry. The extremely rapid formation rate attained in these heat exchangers cannot be controlled, so that a blockage of the flow always limits the operation. In order to use this simpler generator to produce CO_2 hydrate continuously, it is necessary to slow down the formation rate and so to prevent the blockage. Addition of a hydrate inhibitor is proposed to control the hydrate formation process so that the slurry remains pumpable.

Antson et al. (2001) studied the mechanism of type-III AFPs on ice growth. They confirm that type-III AFPs can make energetically favourable interactions with several ice surfaces, in which way inhibiting crystal growth. Kutschan et al. (2014) studied the dynamic mechanism of AFPs on inhibiting of ice growth and derived a correlation of the induction time as a function of concentration. Bagherzadeh et al. (2015) pointed that the ice-binding AFPs can act as a gas hydrate inhibitor. In this work the effect of type-III AFPs on CO_2 hydrate formation rate in a coil heat exchanger was investigated. The experiments were done with various concentrations of AFPs (up to 50 ppm). A hydrate crystal growth model is developed taking the concentration of AFPs into consideration. The experimental results were compared to those obtained using PVP and PVCap which are the leading KHIs on the market and thus serve as a good reference when testing the KHI potential of the AFPs. The results can be used to guide the design of a crystallizer when continuous CO_2 hydrate slurry is to be produced.

2. EXPERIMENTAL METHOD

2.1 Experimental apparatus

The experimental system has previously been utilized by Zhou et al. (2016) to produce TBAB hydrate slurry and it allowed continuous production up to hydrate concentrations OF 40 wt%. Therefore, it's considered that this system could also work for the generation of CO_2 hydrate slurry. Ultra-deionized water is used in this study to exclude the impact of other ions such as Na^+, Mg^{2+} and Cl^-.

2.2 Experimental procedure

Experiments are firstly done with pure water and CO_2 water solution separately to validate the experimental method. The pressure drop and heat transfer coefficient of the coil heat exchanger will firstly be discussed.

The flow phenomena in helically coiled tubes are more complex than in straight tubes due to centrifugal force effects. The transition from laminar to turbulent flow is shifted to higher Reynolds numbers (Kast, 2010):

$$Re_{crit} = 2300\left[1+8.6\left(\frac{d_i}{D_c}\right)^{0.45}\right] \tag{1}$$

For the experimental conditions, $\mathrm{Re_{crit}} = 7437$, for all tests the flow is laminar.

The pressure drop is calculated based on Darcy–Weisbach's equation:

$$\Delta P = \left(f_{str}\frac{L_{str}}{d_i} + f_c\frac{L_c}{d_i} + F_L \right)\frac{\rho\omega^2}{2} \tag{2}$$

In which, the friction factor is obtained with the Poiseuille relation for laminar flow:

$$f_{str} = \frac{64}{Re} \tag{3}$$

Frictional factor for curved tubes in relation to the friction factor for straight tubes is obtained from Naphon and Wongwises (2006):

$$\frac{f_c}{f_{str}} = 1+0.015Re^{0.75}\left(\frac{d_i}{D_c}\right)^{0.4} \tag{4}$$

F_L in Eq. (2) stands for the loss caused by the sharp corners in the tubes. It was determined to be 0.9 (derived from Kast, 2010) for one turn, there are totally 5 turns in the coil tube.

The experimental pressure drop has been compared with the pressure drop derived from Eq. (2) and is shown in Fig. 1. It indicates that the pressure drop of water test can be well predicted. While Eq. (2) always under predicts the experimental value for CO_2 water solution circulation. That is because the saturated CO_2 gas bubbles in the solution increase the pressure drop during circulation and this effect is not taken into account in Eq. (2).

The experimental overall heat transfer coefficient of the system is calculated based on the energy balance that is based on the measured temperatures, pressures and flow rates

$$U_{\exp} = \frac{\dot{m}\Delta i - \dot{m}\dfrac{\Delta P}{\rho_S} - \dot{Q}_{loss}}{A\Delta T_{\ln}} \tag{5}$$

Where $\Delta T_{\ln}$ is defined as

$$\Delta T_{\ln} = \frac{(T_{inlet} - T_{bath}) - (T_{outlet} - T_{bath})}{\ln \dfrac{T_{inlet} - T_{bath}}{T_{outlet} - T_{bath}}} \tag{6}$$

The energy loss in Eq. (5) has been estimated to be equal to 3 W by calculating it from the length of the tube and its insulation thickness.

The heat transfer performance has been derived from Eq. (7)

$$\frac{1}{U} = \frac{1}{h_i} + \frac{d_i \ln \dfrac{d_o}{d_i}}{2\lambda_w} + \frac{d_i}{d_o}\frac{1}{h_o} \tag{7}$$

In which, the internal heat transfer coefficient, h_i, is predicted by Xin and Ebadian (1997). Their correlation is obtained experimentally for the local heat transfer in helical pipes.

$$Nu = (2.153 + 0.318De^{0.643})Pr^{0.177} \tag{8}$$

Eq. (8) is applicable for $20 < De < 2000$, $0.7 < Pr < 175$, $0.0267 < d/D_c < 0.0884$.

The external heat transfer coefficient, h_o, is predicted by Eq. (9), which has been derived in Zhou et al. (2016).

$$h_o = 1.4\dot{Q} + 32 \tag{9}$$

The thermal conductivity of the stainless-steel wall is 13 W m^{-1} K^{-1}.

Fig. 2 shows the comparison of the predicted and experimental overall heat transfer coefficient of CO_2 water solution. It indicates that Eq. (7) under predicts the experimental results, however, the average deviation is within ±10%, which is considered acceptable.

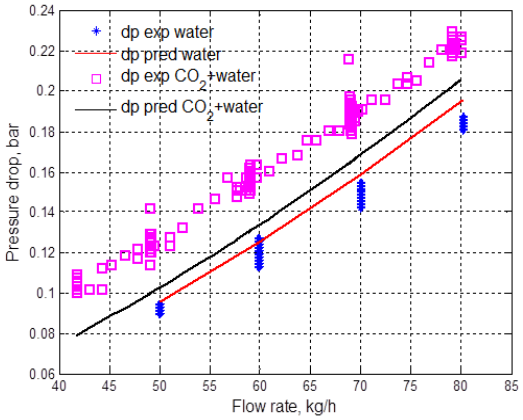

Figure 1: Comparison of the pressure drop of water and CO_2 solution.

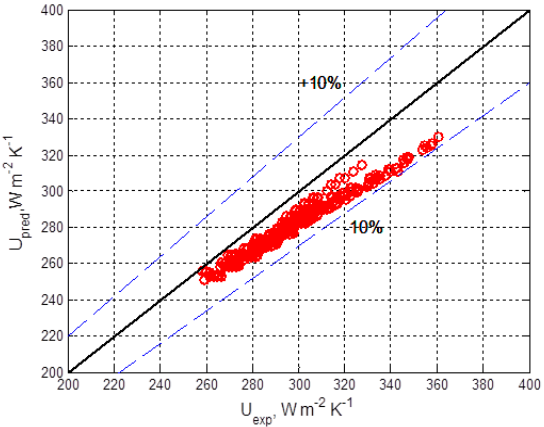

Figure 2: Comparison of the experimental and predicted overall heat transfer coefficient of CO_2 water solution.

After validation, CO_2 water solution with or without the addition of AFPs is filled in the system. The type-III AFP used in the experiments was purchased from A/F Protein Canada Inc. The solution in the coil is cooled by the two thermostatic baths filled with tap water from 10 °C with steps of 0.5 K until there are crystals appearing in the sight glasses. The effective cooling capacity of each bath is 0.3 kW. The warm bath is kept at a temperature higher than the cold bath, in this way, part of the crystals formed in the cold bath are supposed to be melted. In this way it should be possible to keep the concentration of crystals in the solution at the required level.

3. EXPERIMENTAL RESULTS

3.1 Super-cooling degree to initiate hydrate formation

Hydrates formation is a crystallization process. A supersaturation is required normally to initiate crystal formation which can be considered as driving force. Hydrates, in this study, are supposed to form on the tube wall firstly according to the temperature profile shown in Fig. 3. Therefore, the super-saturation degree of hydrate formation is defined as the difference between the wall temperature and the equilibrium temperature of the solution under the same pressure.

$$\Delta T = T_w - T_{eq} \tag{10}$$

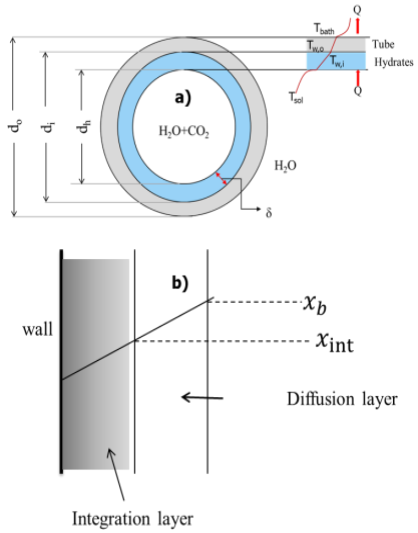

Fig. 3: Crystal layer formation on the tube wall.

Sabil (2009) has experimentally investigated the equilibrium condition of CO_2 hydrate formation. The super-cooling degree of the CO_2 solution to initiate hydrate formation with different concentrations of AFPs has been obtained taking Sabil's phase equilibrium line as reference. Fig. 4a shows the points when hydrates start forming with AFPs added. Symbols marked by 1, 2 and 3 represent the condition with 0, 5 ppm and 10 ppm AFPs respectively. It indicates that without the addition of AFPs, the supercooling degree is only 0.5 K when hydrate started forming, while with the addition of 5 ppm AFPs, 0.8 K supercooling degree is needed to start hydrate formation. When there are 10 ppm AFPs added in the solution, an even larger supercooling degree (ca. 2.75 K) has to be achieved before hydrates start forming. The addition of AFPs increases the required super-saturation degree before hydrate formation can be initiated which means it's more difficult for hydrates to start forming with the addition of type-III AFPs up to 10 ppm.

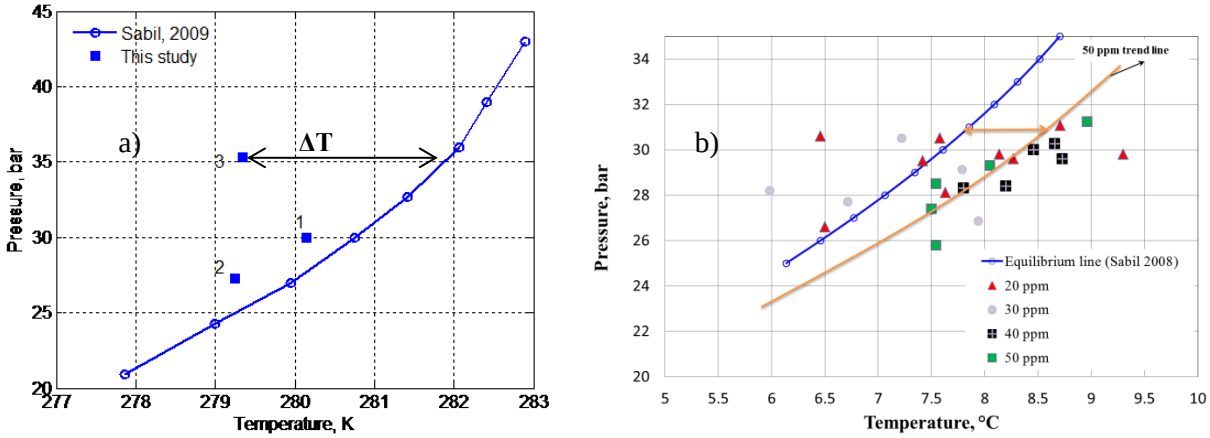

Figure 4: a) Supercooling degree of CO_2 solution under AFPs concentration up to 10 ppm; b) Supercooling degree of CO_2 solution under AFPs concentrations of 20 and 50 ppm;

Fig. 4b shows the cases with the addition of AFPs from 20 ppm to 50 ppm. It illustrates quite different behaviour in comparison with Fig. 4a. The symbols stand for the temperature and corresponding pressure of the wall when hydrates start forming. It illustrates that the symbols for the cases, when the addition of AFPs is higher than 30 ppm, always appear in the right region of the equilibrium line, which means hydrates start forming above the equilibrium condition defined by Sabil (2009) shown in Fig. 4a. While, for the cases with AFPs 20 ppm and 30 ppm, formation can start with positive and negative supersaturation depending on the operating conditions. Thereby, a conclusion has been drawn that the addition of AFPs shifted the hydrate formation equilibrium line to higher temperature when the concentration of AFPs is higher than 30 ppm. Hydrate formation trend line has been drawn for the case of with the addition of 50 ppm AFPs. It indicates a shift of 0.5 K of the equilibrium line for the case of 50 ppm.

3.2 Heat transfer performance under hydrate formation condition

The adhesion of hydrates on the tube wall increases the thermal resistance resulting in an overall heat transfer coefficient given by Eq. (11).

$$\frac{1}{U_h} = \frac{d_i}{d_h}\frac{1}{h_i} + \frac{d_i \ln\frac{d_o}{d_i}}{2\lambda_w} + \frac{d_i \ln\frac{d_i}{d_h}}{2\lambda_h} + \frac{d_i}{d_o}\frac{1}{h_o} \tag{11}$$

In which, the thermal conductivity of CO_2 hydrate solid has been taken as 0.54 W/m K for the relevant temperature range according to the value reported by Sloan and Koh (2008). The thickness of the crystal layer δ can then be derived from Eqs. (5), (7) and (11) to be $\delta=(d_i-d_h)/2$.

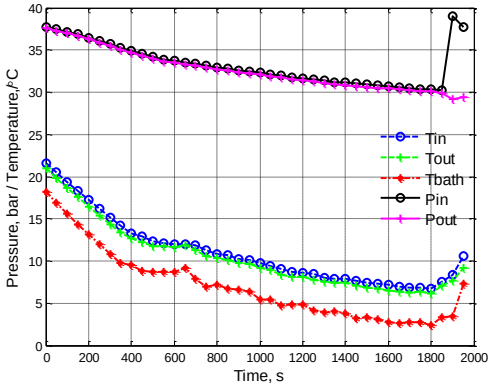

Figure 5: Pressure and temperature change during hydrate formation.

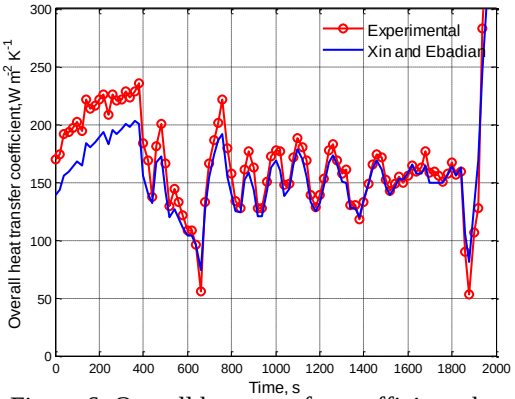

Figure 6: Overall heat transfer coefficient change during hydrate formation.

Fig. 5 shows the temperature change of one test during hydrate formation without the addition of AFPs. The bath temperatures are lowered down gradually until there is a sharp increase of the inlet temperature, which indicates the hydrate formation. The experimental and predicted overall heat transfer coefficients during this period are shown in Fig. 6. From the comparison, in the beginning before hydrates are formed, the experimental overall heat transfer coefficient can be well predicted by the correlation of Xin and Ebadian (1997). There is a sudden decrease of the overall heat transfer coefficient at 9100 s which is consistent with the data of Fig. 5. The experimental overall heat transfer coefficient decreases to zero in the end which indicates the blockage. The adherence of hydrates on the tube wall increases the thermal resistance which results in a sharp decrease of the heat transfer coefficient. Fig. 6 also indicates that without the addition of AFPs there is a rapid blockage after hydrates start forming.

Figs. 7 a~d show the comparison of the experimental and predicted overall heat transfer coefficient during hydrate formation with the addition of 5 ppm, 10 ppm, 20 ppm and 50 ppm. They all show a similar trend. Taking Fig. 7a as an example, it illustrates that from 3050 s there is a sudden decrease of the overall heat transfer coefficient from 180 W m^{-2} K^{-1} to 140 W m^{-2} K^{-1}, and the experimental overall heat transfer coefficient starts being lower than the predicted value, which indicates the formation of hydrates on the wall. It keeps an almost straight line (marked by the dashed-line circle) until a sharp decrease to zero at time 5800 s, which indicates the blockage of the tube.

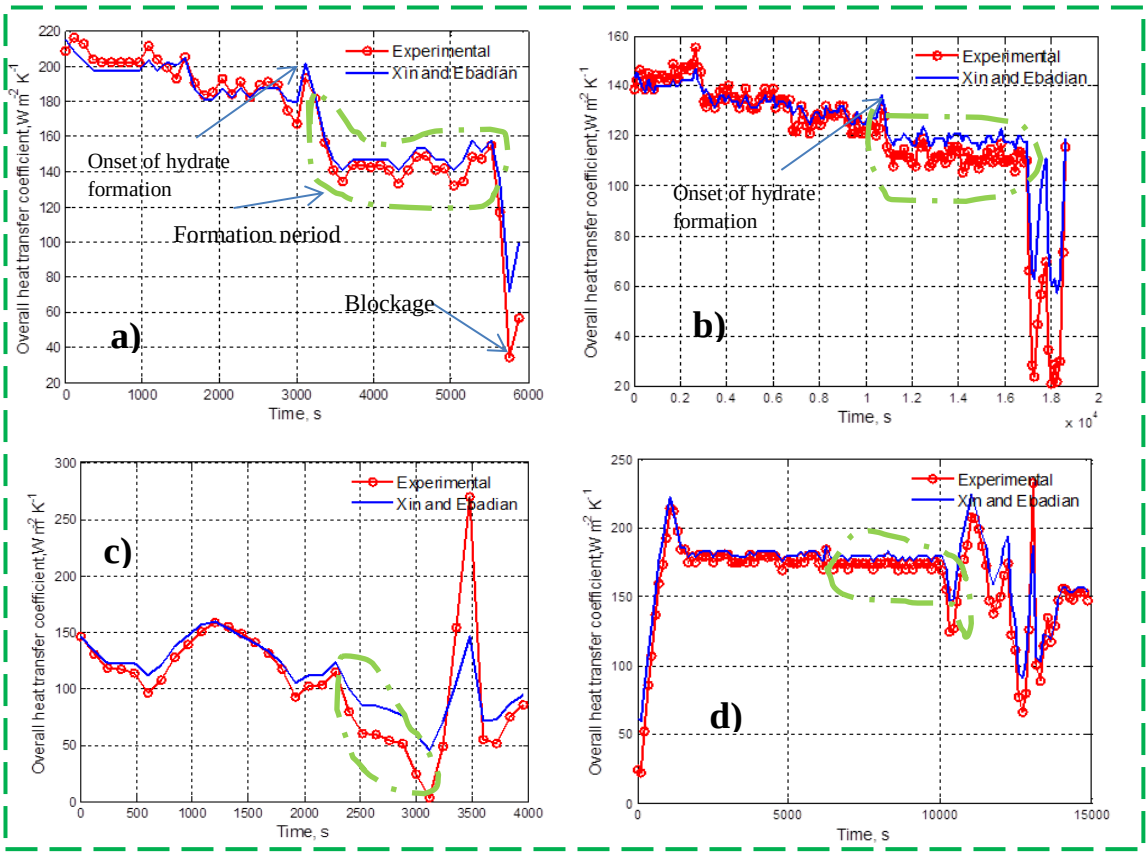

Figure 7: a) Comparison of experimental and predicted overall heat transfer coefficient with the addition of 5 ppm AFPs; b) Comparison of experimental and predicted overall heat transfer coefficient with the addition of 10 ppm AFPs; c) Comparison of experimental and predicted overall heat transfer coefficient with the addition of 20 ppm AFPs; d) Comparison of experimental and predicted overall heat transfer coefficient with the addition of 50 ppm AFPs.

Table 1 shows the length of the formation period before a blockage takes place. The period with 10 ppm is significantly larger than that with 5 ppm AFPs. However, the lasting period for the case with 20 ppm AFPs is shorter than that with 10 ppm AFPs and even shorter than that with 5 ppm AFPs, which is possibly due to the change of

equilibrium condition, which weakened the effect of the additive. The period of operation is the largest for the case with the addition of 50 ppm AFPs.

Table 1: Summary of experimental operation time without blockage

Concentration	Periods
ppm	min
0	—
5	36.7
10	83.3
20	20.0
50	86.7

3.3 Investigation of hydrate growth rate

The experimental growth rate of crystals can be predicted by the change of the internal diameter due to the adherence of solids on the tube wall

$$v = \frac{d_i - d_h}{2\Delta t} \tag{12}$$

Figs. 8a~d show the internal diameter change corresponding with the cases shown in Fig. 7a~d. Fig. 8a shows that the internal diameter starts decreasing from 3050 s. It decreases slowly in the time period from 3400 s to 5600 s followed by a sharp decrease to zero at time 5600 s, which is agreement with Fig. 7a. Figs. 8 b-d are in agreement with Figs. 7 b-d.

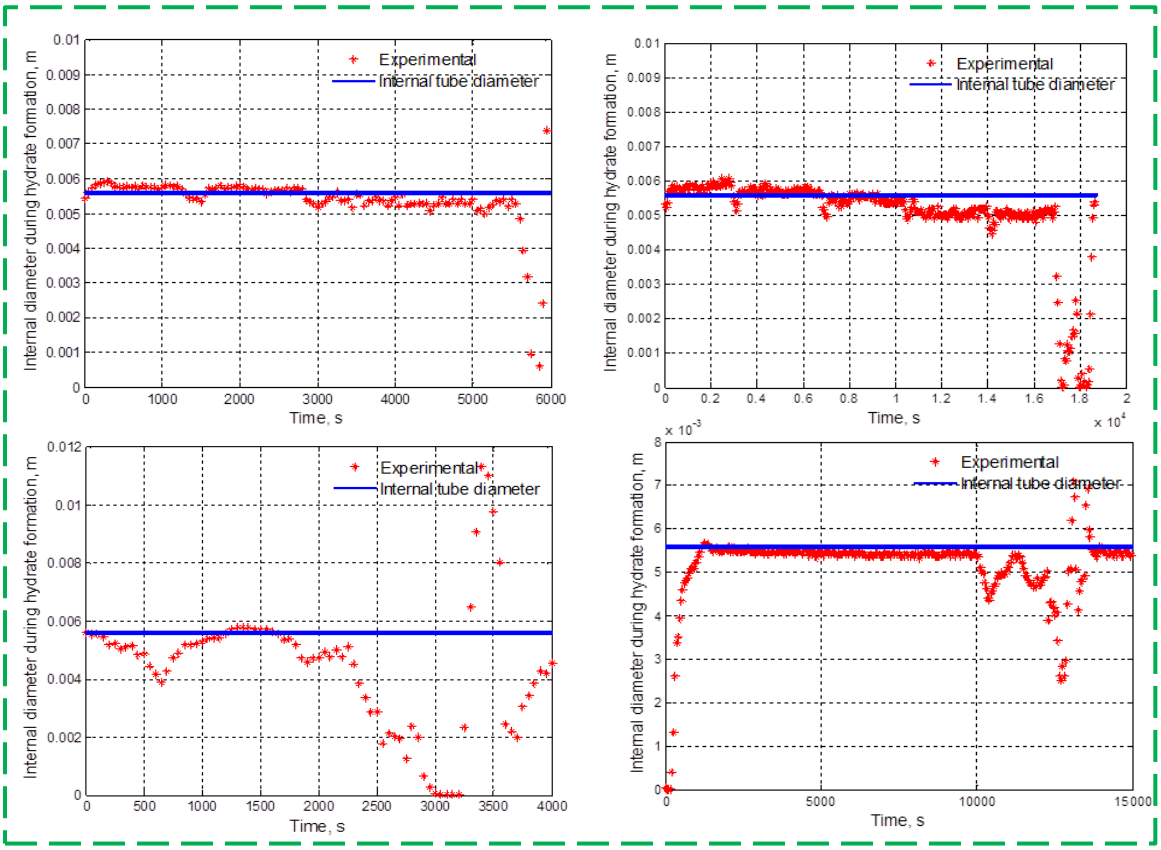

Figure 8: a) Change of internal diameter of the coil during hydrate formation experiment with the addition of 5 ppm AFPs; b) Change of internal diameter of the coil during hydrate formation experiment with the addition of 10 ppm AFPs; c) Change of internal diameter of the coil during hydrate formation experiment with the addition of 20 ppm AFPs; d) Change of internal diameter of the coil during hydrate formation experiment with the addition of 50 ppm AFPs.

Table 2 summarizes the influence of AFPs on CO_2 hydrate formation compared with the results from Uchida et al. (2002) and Shadi et al. (2008). It indicates that the supercooling degree of CO_2 hydrate formation is influenced significantly when the concentration of AFPs is 10 ppm, while with 5 ppm AFPs there was a much smaller effect on the supercooling degree. Even though there is a supercooling-degree of 0.5 K when there is no AFPs addition to the

solution, during this experiment, the hydrate formation cannot be measured because of instantaneous blockage. Table 2 also shows that the hydrate formation rate can only be quantified when there is an addition of AFPs to the solution. The density of CO_2 hydrate slurry is determined to be 1036 kg m^{-3} as measured the same with Zhou et al. (2015). The addition of AFPs significantly lowers the formation rate of the gas hydrate. The growth rate of hydrate with 10 ppm AFPs is only 6.6% of the growth rate with 5 ppm AFPs in the solution. While the growth rate with the addition 50 ppm AFPs is 5.8% of the growth rate with 5 ppm. It should be noticed that 50 ppm the phase change temperature is 0.5 K higher.

Table 2: Summary of experimental results of hydrate growth rate

Concentration of AFPs / ppm	Super-cooling / K	Growth rate (G) / (kg/h)		Formation rate (mm/s)	
		This study	**Shadi et al. (2008)**	This study	Uchida et al. (2002)
0	0.5	—	0.013	—	—
5	0.8	0.1482	—	0.5e-3	0.519
10	2.75	0.00978	—	0.033e-3	3.63
20		0.1897		0.64e-3	
50		0.00859		0.029e-3	
35 （Poly VP/VC）	—	—	0.0105	—	—
70	—	—	0.0095	—	—

4. DEVELOPMENT OF CRYSTAL GROWTH MODEL

Gas hydrate formation is a crystallization process, which requires a certain supersaturation degree to initiate the crystal formation as illustrated in the experiments reported in Fig. 4. Without any addition of inhibitor, 0.5 K super cooling degree is required to initiate hydrate formation.

In this study, the CO_2 gas is supposed to be supersaturated in the bulk aqueous phase, the diffusion rate of CO_2 gas from bulk aqueous phase to the interface of water-hydrate (diffusion layer in Fig. 3b) is considered to be the rate controlling step. The tube wall is assumed to be uniform in temperature. Therefore, the crystal layer forms along the tube wall and increases to a thickness of δ. A modified Skovborg and Rusmussen (1994) model is developed to describe the crystal growth mechanism depicted in Fig. 3b.

$$G = k\rho_{sol}A_i(x_{\text{int}} - x_b) \tag{13}$$

Where k is the mass transfer coefficient of CO_2 gas from the water phase to the interface of water-hydrate. In the present study this is the internal surface of the crystal layer which grows inside the coil. It can be obtained from Eq. (14).

$$k = \frac{Sh\text{Đ}}{d_i - 2\delta} \tag{14}$$

In which the Sherwood number is predicted making use of the analogy with heat transfer correlations from Edwards et al. (1979) for laminar flow

$$Sh = 3.66 + \frac{0.065(d_i / L_c)\,\mathrm{Re}\,Sc}{1 + 0.04[(d_i / L_c)\,\mathrm{Re}\,Sc]^{2/3}} \tag{15}$$

The concentration of CO_2 in the bulk water under the supersaturation condition can be derived from the equation of Diamond and Akinfiev (2003).

The crystal layer thickness δ keeps increasing and thus the slurry velocity will also increase according to the conservation of mass until the friction between the slurry and the crystal layer is high enough causing detachment of crystals from the layer into the slurry. At this point, the mass of crystals that are formed at the layer is equal to the mass of crystals that are transported to the slurry and the crystal layer thickness is constant.

The experimental growth rate derived from Eq. (12) is used to calculate the mass transfer coefficient *k* in Eq. (13). The diffusion coefficient *Đ* of CO_2 in the solution can then be derived from Eq. (14), in which, the crystal thickness δ for each case is the value derived during the hydrate formation period pointed in Figs. 7a and 7b. The results are shown in Table 3. It shows that the diffusion coefficient of CO_2 in the solution is significantly reduced as the concentration of AFPs increases, the diffusion coefficient with the addition of 10 ppm AFPs is 44 times lower than that with the addition of 5 ppm AFPs. Resulting an extreme reduction of mass transfer coefficient (17 times lower when the concentration of AFPs is 10 ppm). Table 3 also indicates that the diffusion coefficient for the cases with AFPs higher than 20 ppm is not predictable because of the negative driving force shown in Fig. 4b. The results indicate that the addition of AFPs prevents the movement of CO_2 gas to the interface of liquid-crystal (in the diffusion layer shown in Fig. 2b). As the amount of free gas reduces, the hydrate formation is slowed down from the reaction balance shown in Eq. (16).

$$CO_2 + N_W H_2O \leftrightarrow CO_2 \cdot N_W H_2O \tag{16}$$

Table 3 Diffusion coefficient derived from experiments

x_{AFPs}	T_{int} /°C	T_b /°C	x_{int} /(mol %)	x_b /(mol %)	δ/(m s^{-1})	k/(m s^{-1})	Đ/(m^2 s^{-1})
0	7.55	7.05	2.507	2.427	—	—	—
5 ppm	6.45	6.15	2.317	2.286	0.005	1.6×10^{-5}	6.0339×10^{-7}
10 ppm	8.35	6.2	2.64	2.29	0.007	9×10^{-7}	4.1736×10^{-9}

5. CONCLUSION

The addition of Type-III AFPs changes the CO_2 hydrate formation behaviour. With the addition of 10 ppm AFPs in weight percent, the supercooling degree is increased significantly compared with that without the addition of AFPs. The addition of 5 ppm AFPs has a much smaller effect. With concentration of AFPs higher than 20 ppm, CO_2 hydrate formation equilibrium line moves to higher temperature. The diffusion coefficient in the cases with 20 ppm and 50 ppm AFPs cannot be derived without the determination of the new equilibrium line.

With the addition of 5 ppm and 10 ppm AFPs, the hydrate growth rate can be better determined from the experimental data. In the case without the addition of AFPs the growth rate is too large so that its rate cannot be determined from the present experiments. With the addition of 10 ppm AFPs, the hydrate growth rate is 6.6% of that of 5 ppm AFPs. The growth rate with the addition 50 ppm AFPs is 5.8% of that of 5 ppm. The gas diffusion coefficient is significantly reduced with the addition of AFPs, in particularly with the addition of 10 ppm AFPs, the gas diffusion rate is 44 times lower than that with the addition of 5 ppm AFPs, resulting in a 17 times lower mass transfer coefficient.

NOMENCLATURE

A	Area	m^2	*v*	Film growth rate	m s^{-1}
d	Diameter	m	*ρ*	Density	kg m^{-3}
Đ	Diffusion coefficient	m^2 s^{-1}	ω	Velocity	m s^{-1}
D_c	Coil diameter	m	**Subscript**		
De	Dean number ($\text{Re}\sqrt{\frac{d}{D_c}}$)		*bath*	Bath	
f	Friction factor		*b*	Bulk	
F	Energy loss		*c*	Coil	
G	Growth rate	kg h^{-1}	*crit*	Critical	
h	Heat transfer coefficient	W m^{-2} K^{-1}	*eq*	Equilibrium	
i	Enthalpy	J kg^{-1}	*exp*	Experimental	

k	Mass transfer coefficient	m s^{-1}	*g-l*	Gas to liquid
L	Length	m	*h*	Hydrate
$\dot{m}$	Mass flow rate	kg s^{-1}	*i*	Inner
N	Number of water moles		*inlet*	Inlet
Nu	Nusselt number		*int*	interfacial
pred	Predicted		*ln*	Logarithmic
P	Pressure	Pa	*loss*	Loss
Pr	Prandtl number		*L*	Local
$\dot{Q}$	Energy flow	J s^{-1}	*o*	Outer
Re	Reynolds number		*outlet*	Outlet
Sc	Schmidt number		*s*	Slurry
Sh	Sherwood number		*sol*	Solution
T	Temperature	K	*str*	Straight
t	Time	s	*w*	Wall
U	Overall heat transfer	W m^{-2} K^{-1}	*W*	Water
x	Molar concentration	mol mol^{-1}	**Abbreviations**	
Greek			*AFP*	Anti-Freeze Proteins
Δ	Difference		*KHIs*	Kinetic Hydrate Inhibitors
δ	Crystal layer thickness	m	*LHTS*	Latent Heat Thermal Storage
λ	Thermal conductivity	W m^{-1} K^{-1}	*PCM*	Phase Change Material
μ	Viscosity	Pa·s	*PVCap*	Polyvinyl Caprolactam
			PVP	Polyvinyl Pyrrolidone

REFERENCES

Antson A.A., Smith D.J., Roper D.I., Lewis S., Caves L.S.D., Verma C.S., Buckley S.L., Lillford P.J., Hubbard R.E., 2001. Understanding the mechanism of ice binding by type III antifreeze proteins. Journal of Molecular Biology, 305 (4), 875-889.

Ayel, V., Lottin, O., Peerhossaini, H., 2003. Rheology, flow behaviour and heat transfer of ice slurries: a review of the state of the art. *Int. J. Refrig*., 26, 95-107.

Bagherzadeh S.A., Alavi S., Ripmeester J.A., Englezos P., 2015. Why ice binding type I antifreeze protein acts as a gas hydrate crystal inhibitor. *Phys. Chem. Chem. Phys*., 17, 9984-9990.

Bel, O., Lallemand, A., 1999. Study of a two phase secondary refrigerant intrinsic thermophysical properties of an ice slurry. *Int. J. Refrig*., 22, 164–74.

Diamond, L.W., Akinfiev, N.N., 2003. Solubility of CO_2 in water from -1.5 to 100 °C and from 0.1 to 100 MPa: evaluation of literature data and thermodynamic modelling. *Fluid Phase Equilib.*, 208, 265-290.

Edwards, D.K., Denny, V.E., Mills, A.F., 1979. *Transfer Processes*, 2nd ed., Hemisphere, Washington, D.C.

Kast W., 2010. Pressure drop in single phase flow in pipes. Heat Atlas VDI Second Edition 2010. Springer.

Kauffeld, M., Christensen, K.G., Lund, S., Hansen, T.M., 1999. Experience with Ice Slurry, Proc. of the 1st workshop on Ice Slurries. Yverdon-les-Bains, Switzerland, IIR, 42-73.

Kutschan B., Morawetz K., Thoms S., 2014. Dynamical mechanism of antifreeze proteins to prevent ice growth. Phys. Rev. E 90, 022711.

Matsumoto, K., Namiki, Y., Okada, M., Kawagoe, T., Nakagawa, S., Kang, C., 2004. Continuous ice slurry formation using a functional fluid for ice storage. *Int. J. Refrig*., 27, 73–81.

Naphon P., Wongwises S., 2006. A review of flow and heat transfer characteristics in curved tubes. *Renew. Sust. Energ. Rev*., 10, 463-390.

Sabil K.M., 2009. Phase behaviour, thermodynamics and kinetics of clathrate hydrate systems of carbon dioxide in presence of tetrahydrofuran and electrolytes. PhD thesis, TU Delft.

Shadi AI-Adel, John A.G. D, Rasha E.G., Phillip S., 2008. The effect of biological and polymeric inhibitors on methane gas hydrate growth kinetics. *Fluid Phase Equilib*., 267, 92-98.

Skovborg P., Rusmussen P., 1994. A mass transport limited model for the growth of methane and the ethane gas hydrates. *Chem. Eng. Sci*., 49, 1131-1143.

Sloan ED., Koh C., 2008. Clathrate hydrates of natural gases. Taylor & Francis.

Tanino, M., Kozawa, Y., 2001. Ice–water two-phase flow behavior in ice heat storage systems. *Int. J. Refrig*., 24, 639–651.

Uchida, T., Ikeda, I.Y., Ebinuma, T., Nagao, J., Narota, H., 2002. CO_2 hydrate film formation at the boundary between CO_2 and water: effects of temperature, pressure and additives on the formation rate. *J. Cryst. Growth*, 383-387.

Xin R. C., Ebadian M.A., 1997. The effects of Prandtl numbers on local and average convective heat transfer characteristics in helical pipes. *Int. J. Heat Fluid Flow*, 18, 482-488.

Zhou H., de Sera I.E.E., Infante Ferreira C.A., 2015. Modelling and experimental validation of a fluidized bed based CO_2 hydrate cold storage system. *Appl. Energy*, 158, 433-445.

Zhou H., Vasilescu C., Infante Ferreira C.A., 2016. Heat transfer and flow characteristics during the formation of TBAB hydrate slurry in a coil heat exchanger. *Int. J. Refrig*., 64, 130-142.

ACKNOWLEDGEMENTS

The authors would like to thank KoudeGroep Delft/Wageningen for their financial support. Hongxia Zhou would like to thank Guangzhou Elites Projects of the Guangzhou Municipal Government for their financial support.